AIAA JOURNAL
Vol. 39, No. 1, January 2001

Effects of Angle of Attack on Nonlinear Flutter of a Delta Wing

Deman Tang* and Earl H. Dowell†
Duke University, Durham, North Carolina 27708-0300

Limit cycle oscillations (LCOs) have been observed in flight for certain modern high-performance aircraft. The nonlinear physical mechanism responsible for the LCOs is still in doubt, even to the point of it not yet being determined whether the nonlinearity is principally in the flexible elastic structure of the aircraft or due to the fluid behavior in the surrounding aerodynamic flowfield. One observation from flight tests is that by changing the angle of attack of aircraft, the flight velocity at which LCOs begin may be raised or lowered and that the amplitude of the LCOs may be reduced. It has been suggested that this sensitivity to angle of attack indicates the nonlinearity is in the fluid rather than in the structure. We show that such effects of an angle of attack change can be the result of a structural nonlinearity. Specifically, an investigation to determine the effects of a steady angle of attack on nonlinear flutter and LCO of a delta wing-plate model in low subsonic flow has been made. A three-dimensional time domain vortex lattice aerodynamic model and a reduced order aerodynamic technique were used, and the structure is modeled using von Kármán plate theory that allows for geometric strain-displacement nonlinearities in the delta wing structure. The results provide new insights into nonlinear aeroelastic phenomena not previously widely appreciated, i.e., LCOs for low aspect ratio wings that have a platelike nonlinear structural behavior. The effects of a steady angle of attack on both the flutter boundary and the LCOs are found to be significant. For a small steady angle of attack, $\alpha_0 \leq 0.1$ deg, the flutter onset velocity increases, whereas for larger α_0, it decreases. Moreover, as α_0 increases, the maximum LCO amplitude decreases substantially. Such effects have been observed by Bunton and Denegri in flight flutter experiments. It is noted that the present theoretical results do not prove that the LCOs phenomena observed in flight are due to structural nonlinearities; however, the results of the present analysis are consistent with those observed in flight and do show that a structural nonlinearity can give rise to the observed effects of angle of attack on the LCOs.

Nomenclature

a_i, b_j	=	generalized coordinates in the x and y directions, respectively
c	=	delta wing root chord
D	=	delta wing plate bending stiffness
E	=	Young's modulus
h	=	delta wing plate thickness
km, kn	=	numbers of vortex elements on a delta wing in the x and y directions, respectively
kmm	=	total number of vortices on both the delta wing and wake in the x direction
L	=	delta wing span
m	=	delta wing panel mass/area, $m = h\rho_m$
mxy	=	number of delta wing modal functions in the x–y plane defining u and v
nxy	=	number of delta wing modal functions in the z-direction defining w
Q^{ij}	=	generalized aerodynamic force
q_n	=	generalized coordinate in the z direction
R_a	=	size of reduced order aerodynamic model
t	=	time
U	=	airspeed
U_f	=	flutter airspeed
U_i, V_j	=	modal functions in x and y directions
u, v	=	in-plane displacements
W_k	=	transverse modal function in the z direction
w	=	plate transverse deflection
X, Y	=	right and left eigenvector matrices of vortex lattice eigenvalue model
x, y	=	streamwise and spanwise coordinates
Z	=	eigenvalue matrix of vortex lattice aerodynamic model
z	=	normal coordinate
z_i	=	discrete time eigenvalue
α_0	=	steady angle of attack
Γ	=	the vortex strength
Δt	=	the time step, $\Delta x / U$
Δx	=	plate element length in the streamwise direction
λ_i	=	continuous time eigenvalues, $\lambda_i = \ell n(z_i)/\Delta t$
ν	=	Poisson's ratio
ρ_∞, ρ_m	=	air and plate densities
τ	=	time parameter, $\sqrt{(mc^4/D)}$, s
ω	=	frequency
$(\dot{})$	=	$\mathrm{d}(\,)/\mathrm{d}t$

Received 15 November 1998; revision received 5 April 2000; accepted for publication 26 April 2000. Copyright © 2000 by the American Institute of Aeronautics and Astronautics, Inc. All rights reserved.

*Research Associate, Department of Mechanical Engineering and Materials Science. Member AIAA.

†J. A. Jones Professor, Department of Mechanical Engineering and Materials Science. Fellow AIAA.

I. Introduction

FLUTTER and limit cycle oscillation (LCO) characteristics of cantilevered low-aspect-ratio rectangular and delta wing models in low subsonic flow speeds have been recently studied. Theoretical and experimental results[1–3] have provided good physical understanding of the relevant phenomena. In particular, it has been demonstrated that, even with only a single edge of a plate restrained, bending tension or geometrical nonlinearities can produce LCO amplitudes of the order of the structural plate thickness. As shown in Ref. 3, a comparison of theory with experiment gives reasonably good agreement. However, some differences exist that may be due to a steady nonzero angle of attack of the delta wing plates. To estimate the effects of the initial angle of attack on the flutter boundary and LCO characteristics, a theoretical and numerical investigation has been made.

In the present paper we use a three-dimensional time domain vortex lattice aerodynamic model and reduced order aerodynamic technique to investigate the flutter and limit cycle oscillation characteristics of a low aspect ratio delta wing plate at low subsonic flow speeds for different steady angles of attack. A perturbation flutter equation was derived that is used to determine the flutter boundary, and a direct time marching solution is used to calculate the LCO behavior of this nonlinear system. The results provide additional

insight with respect to the LCOs of cantilevered low-aspect-ratio wing-panel models.

II. State-Space Equations

A schematic of the delta wing plate geometry with a three-dimensional vortex lattice model of the unsteady flow is shown in Fig. 1. The aeroelastic structure/fluid state-space equations are described as follows.

The nonlinear structural equations were derived from Lagrangian equations based on the von Kármán plate equations using the total kinetic and elastic energies and the work done by applied aerodynamic loads on the plate. Modal expansions for the plate deflection are substituted into the energy expressions and then into Lagrangian equations to yield equations of motion for each structural modal coordinate. The modal functions used are the in-plane and out-of-plane natural modes of the plate determined from a finite element analysis. As shown in Ref. 3, the nondimensional in-plane (u, v) equation in matrix form is (note the in-plane inertia has been neglected)

$$\begin{pmatrix} C^u & C^v \\ D^u & D^v \end{pmatrix} \begin{Bmatrix} a_i \\ b_j \end{Bmatrix} = \begin{pmatrix} C^q \\ D^q \end{pmatrix} \{q_k q_m\} \tag{1}$$

The nondimensional transverse equation is

$$\sum_m M_m^k \left[\ddot{q}_m + 2\omega_m \xi_m \dot{q}_m + \omega_m^2 q_m\right] + \left(F_N^k \middle| \tau^2\right) + (Q^k/\tau^2) = 0 \tag{2}$$

where M_m^k are generalized modal masses, ξ_m and ω_m are the mth structural modal damping and natural frequency, Q^k is the nondimensionalized generalized aerodynamic force, and F_N^k is a (nondimensional) force vector (linear and nonlinear) that depends on the deflection of the delta plate. This vector can be expressed in matrix form as

$$\{F_N\} = [\Pi^1] \begin{Bmatrix} a_i q \\ b_j q \end{Bmatrix} + [\Pi^2]\{q_k q_m q_n\} \tag{3}$$

where $i, j = 1, 2, \ldots, mxy$ and $k, m, n = 1, 2, \ldots, nxy$. For details of the coefficient matrices, C^u, C^v, D^u, D^v, C^q, Π^1, and Π^2, see the Appendix.

It should be noted that the structural model used here is appropriate to a platelike structure that undergoes bending in two directions, e.g., chord and span. This bending leads to nonlinear effects for deflections of the order of the plate thickness. For a beamlike structure, e.g., a high-aspect-ratio wing, this nonlinear effect is much weaker. Then the deflections required to reach a nonlinear state are much larger, and, moreover, other nonlinear effects may become important, e.g., nonlinear curvature.

An unsteady vortex lattice method was used to calculate the aerodynamic forces. The flow is assumed to be incompressible, inviscid, and irrotational. A typical planar vortex lattice mesh for the three-dimensional flow is shown in Fig. 1. The plate and wake are divided into a number of elements. In the wake and on the wing, all the elements are of equal size, Δx, in the streamwise direction. Point vortices are placed on the plate and in the wake at the quarter chord of the elements. At the three-quarter chord of each plate element, a collocation point is placed for the downwash, i.e., we require the velocity induced by the discrete vortices to equal the downwash arising from the unsteady motion of the delta wing. As described in Ref. 4, the aerodynamic matrix equation can be expressed as

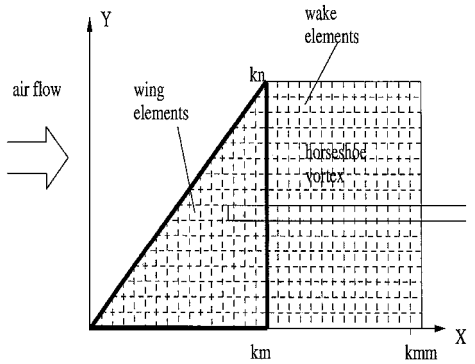

Fig. 1 Numerical grid for delta wing plate using vortex lattice aerodynamic model and a corresponding finite element grid for the structural model.

$$[A]\{\Gamma\}^{t+1} + [B]\{\Gamma\}^t = [T]\{w\}^{t+1} \tag{4}$$

where $[A]$ and $[B]$ are aerodynamic coefficient matrices,[4] $[T]$ is a transfer matrix for determining the relationship between the global vortex lattice mesh and local vortex lattice mesh on the delta wing plate, and $\{w\}^{t+1}$ is the nondimensional downwash at the time step $t+1$ arising from the unsteady motion and the steady angle of attack of the delta wing. The downwash is expressed in matrix form as

$$\{w(x,y)\}^{t+1} = \frac{h}{U}[W(x,y)]\{\dot{q}\}^{t+1} + \frac{h}{c}\left(\frac{\partial W(x,y)}{\partial x}\right)\{q\}^{t+1} + \{\alpha_0(x,y)\} \tag{5}$$

Thus, combining Eqs. (1), (2), and (4), we obtain a complete aeroelastic state-space equation in matrix form:

$$\begin{pmatrix} A & -TE \\ C_2 & D_2 \end{pmatrix} \begin{Bmatrix} \Gamma \\ \boldsymbol{\theta} \end{Bmatrix}^{t+1} + \begin{pmatrix} B & 0 \\ C_1 & D_1 \end{pmatrix} \begin{Bmatrix} \Gamma \\ \boldsymbol{\theta} \end{Bmatrix}^t = \begin{Bmatrix} T\alpha_0 \\ -\boldsymbol{F}_N \middle| \tau^2 \end{Bmatrix}^{t+\frac{1}{2}} \tag{6}$$

where the vector $\boldsymbol{\theta}$ is the state of the plate $\{\boldsymbol{\theta}\} = \{\dot{q}, q\}^T$, D_1 and D_2 are matrices describing the plate structural behavior, and C_1 and C_2 are matrices describing the vortex element behavior on the delta wing itself.

Based on Eq. (6), a reduced order aerodynamic model with static correction technique is applied. The final result is given by[2–4]

$$\begin{pmatrix} I & -Y_{\mathrm{Ra}}^T[I - A(A+B)^{-1}]TE \\ C_2 X_{\mathrm{Ra}} & D_2 + C_2(A+B)^{-1}TE \end{pmatrix} \begin{Bmatrix} \gamma_d \\ \boldsymbol{\theta} \end{Bmatrix}^{t+1} + \begin{pmatrix} -Z_{\mathrm{Ra}} & Y_{\mathrm{Ra}}^T B(A+B)^{-1}TE \\ C_1 X_{\mathrm{Ra}} & D_1 + C_1(A+B)^{-1}TE \end{pmatrix} \begin{Bmatrix} \gamma_d \\ \boldsymbol{\theta} \end{Bmatrix}^t = \begin{Bmatrix} 0 \\ -(C_1+C_2)(A+B)^{-1}T\alpha_0 - \boldsymbol{F}_N \middle| \tau^2 \end{Bmatrix}^{t+\frac{1}{2}} \tag{7}$$

where X_{Ra} and Y_{Ra} are the right and left reduced eigenvector matrices, Z_{Ra} is a reduced diagonal matrix whose diagonal entries contain the aerodynamic eigenvalues, and γ_d is a reduced vector of the aerodynamic modal coordinates.

III. Nonlinear and Perturbation Flutter Equations

Equation (7) is a nonlinear equation. For a zero steady angle of attack, i.e., $\alpha_0 \equiv 0$, a linear flutter boundary is determined using Eq. (7) by setting $\boldsymbol{F}_N = 0$, as shown in Ref. 3. The limit cycle motion amplitude approaches zero when the flow velocity approaches the linear flutter velocity from above and tends to a finite amplitude LCO when the flow velocity is higher than the linear flutter velocity.

For $\alpha_0 \neq 0$, a perturbation approach is used to determine the linear flutter boundary.

Let

$$q = \bar{\boldsymbol{q}} + \hat{q}, \qquad a_i = \bar{\boldsymbol{a}}_i + \hat{a}_i$$
$$b_j = \bar{\boldsymbol{b}}_j + \hat{b}_j, \qquad \gamma_d = \bar{\gamma}_d + \hat{\gamma}_d \tag{8}$$

where $\bar{\boldsymbol{q}}, \bar{\boldsymbol{a}}_i, \bar{\boldsymbol{b}}_j$, and $\bar{\gamma}_d$ are the static equilibrium state vectors and the corresponding quantities with a symbol of $\hat{}$ are the small dynamic perturbations about the static equilibrium state.

Substituting the Eq. (8) into Eq. (7), a set of static equilibrium equations and dynamic perturbation equations is obtained. For the static equilibrium equations, we have

$$\{\bar{\gamma}_d\}^{t+1} = \{\bar{\gamma}_d\}^t = \{\bar{\gamma}_d\}$$

$$\{\bar{\theta}\}^{t+1} = \{\bar{\theta}\}^t = \{\bar{\theta}\} = \begin{Bmatrix} 0 \\ \bar{\boldsymbol{q}} \end{Bmatrix}$$

The static equilibrium equations are expressed as

$$\left[D_1 + D_2 + (C_1 + C_2)(A + B)^{-1}TE\right]\{\bar{\theta}\} = \left\{-(C_1 + C_2)(A + B)^{-1}T\alpha_0 - \bar{\boldsymbol{F}}_N \mid \tau^2\right\} \tag{9}$$

where

$$\{\bar{\boldsymbol{F}}_N\} = [\Pi^1]\begin{Bmatrix}\bar{a}_i\bar{\boldsymbol{q}}\\ \bar{b}_j\bar{\boldsymbol{q}}\end{Bmatrix} + [\Pi^2]\{\bar{\boldsymbol{q}}_k\bar{\boldsymbol{q}}_m\bar{\boldsymbol{q}}_n\}$$

$$\begin{pmatrix}C^u & C^v\\ D^u & D^v\end{pmatrix}\begin{Bmatrix}\bar{a}_i\\ \bar{b}_j\end{Bmatrix} = \begin{pmatrix}C^q\\ D^q\end{pmatrix}\{\bar{\boldsymbol{q}}_k\bar{\boldsymbol{q}}_m\}$$

It is evident that Eq. (9) is a set of nonlinear algebraic equations for the unknown state vectors $\{\bar{\boldsymbol{q}}\}$, $\{\bar{a}_i\}$, and $\{\bar{\boldsymbol{b}}_j\}$.

The dynamic perturbation equations about a static equilibrium state are

$$\begin{pmatrix}I & -Y_{\mathrm{Ra}}^T[I - A(A + B)^{-1}]TE\\ C_2X_{\mathrm{Ra}} & D_2 + C_2(A + B)^{-1}TE\end{pmatrix}\begin{Bmatrix}\hat{\gamma}_d\\ \hat{\theta}\end{Bmatrix}^{t+1} + \begin{pmatrix}-Z_{\mathrm{Ra}} & Y_{\mathrm{Ra}}^TB(A + B)^{-1}TE\\ C_1X_{\mathrm{Ra}} & D_1 + C_1(A + B)^{-1}TE\end{pmatrix}\begin{Bmatrix}\hat{\gamma}_d\\ \hat{\theta}\end{Bmatrix}^{t} = \begin{Bmatrix}0\\ -(\hat{F}_L + \hat{F}_N)\mid \tau^2\end{Bmatrix}^{t+\frac{1}{2}} \tag{10}$$

where $\hat{F}_L$ and $\hat{F}_N$ are the linear and nonlinear perturbation forces, respectively:

$$\{\hat{F}_L\} = [\Pi^1]\left(\begin{bmatrix}|\\ \phi(\bar{a}_i, \bar{\boldsymbol{b}}_j)\\ |\end{bmatrix}\{\hat{q}\} + \begin{bmatrix}|\\ \psi_1(\bar{\boldsymbol{q}}_k)\\ |\end{bmatrix}\begin{Bmatrix}\hat{a}_i\\ \hat{b}_j\end{Bmatrix}\right) + [\Pi^2]\begin{bmatrix}|\\ \psi_2(\bar{\boldsymbol{q}}_k\bar{\boldsymbol{q}}_m)\\ |\end{bmatrix}\{\hat{q}\}$$

$$\begin{pmatrix}C^u & C^v\\ D^u & D^v\end{pmatrix}\begin{Bmatrix}\hat{a}_i\\ \hat{b}_j\end{Bmatrix} = \begin{pmatrix}C^q\\ D^q\end{pmatrix}\begin{bmatrix}|\\ \psi_1(\bar{\boldsymbol{q}}_k)\\ |\end{bmatrix}\{\hat{q}\}$$

or

$$\{\hat{F}_L\} = [K_d]\{\hat{q}\}$$

where $[K_d]$ is an additional structural stiffness matrix due to the nonlinear static deflection that depends upon the flow velocity. The total structural stiffness (or "structural" natural frequencies) will change with the flow velocity.

The nonlinear perturbation force is

$$\{\hat{F}_N\} = [\Pi^1]\begin{Bmatrix}\hat{a}_i\hat{q}\\ \hat{b}_j\hat{q}\end{Bmatrix} + [\Pi^2]\begin{bmatrix}|\\ \psi_3(\bar{\boldsymbol{q}}_k)\\ |\end{bmatrix}\{\hat{q}_m\hat{q}_n\} + [\Pi^2]\{\hat{q}_k\hat{q}_m\hat{q}_n\}$$

If we set $\hat{F}_N = 0$, then a linear perturbation flutter equation is given by

$$[\mathcal{A}]\begin{Bmatrix}\hat{\gamma}_d\\ \hat{\theta}\end{Bmatrix}^{t+1} + [\mathcal{B}]\begin{Bmatrix}\hat{\gamma}_d\\ \hat{\theta}\end{Bmatrix}^{t} = \{0\} \tag{11}$$

The coefficient matrices $[\mathcal{A}]$ and $[\mathcal{B}]$ are dependent on the static equilibrium state. For the details of these coefficient matrices, see the Appendix.

To determine the LCO response of this nonlinear aeroelastic system, we can use Eq. (10) and a time marching approach.

IV. Numerical Results

The theoretical model is a simple delta wing configuration with a leading edge sweep of 45 deg. The model was constructed from 2.38-mm-thick plastic (Lucite material) plate. The root chord was locally clamped (cantilevered) and the length of the cantilever root was 0.228 m (60% root chord). The clamping was symmetric about the center of the root chord of the model. The length of the root chord was 0.381 m. We use the aerodynamic vortex lattice model including 120 vortex elements on the delta wing ($km = kn = 15$), 525 vortex elements in the wake ($kmm = 50$), and nine reduced aerodynamic eigenmodes $R_a = 9$. The delta wing structural modal numbers were $nxy = 10$ in the out-of-plane and $mxy = 10$ in the in-plane directions, respectively. The mesh of the finite element model for the out-of plane structural model is 30×30, and, thus, the delta wing was modeled using 900 quadrilateral plate elements. The mesh of the three-dimensional finite element model for the in-plane structural model is $30 \times 30 \times 1$, and the delta wing was modeled using 961 solid elements with 1921 nodes. The nodes at the clamped root chord satisfy geometric boundary conditions, i.e., $w = u = v = \theta_x = \theta_y = \theta_z = 0$.

A. Nonlinear Flutter

In the following calculation we consider a range of steady angle of attack, i.e., from $\alpha_0 = 0$ to 2 deg. For the static equilibrium state, we use Eq. (7) and a time marching approach to calculate directly nonlinear response. The static state vectors $\{\bar{\boldsymbol{q}}\}$, $\{\bar{\boldsymbol{a}}\}$ and $\{\bar{\boldsymbol{b}}\}$ are extracted from the static part of steady time response. Of course, these can also be obtained from Eq. (9), but for larger mxy and nxy, this equation is tedious to solve.

1. *Results for $\alpha_0 = 0.1$ deg*

The static plate transverse deflection increases as the flow velocity increases, and the structural natural frequencies also change. In computing the "structural" natural frequency, we take into account the aerodynamic forces in computing the static deflections but ignore them in the dynamic perturbation analysis. The results are shown in Fig. 2 for the first five structural natural frequencies vs the flow velocity from 0 to 48 m/s. In this case, the frequencies increase with the increasing flow velocity. Note that the first five structural natural frequencies at $U = 0$ are 7.46, 29.58, 33.81, 70.21, and 83.72 Hz. For example, the frequency increases are 53, 13, and 19%, respectively, for the first three frequencies at $U = 38$ m/s compared with at $U = 0$. The "structural frequencies" could be measured experimentally if we replaced the static aerodynamic forces with equivalent mechanical loads and performed an in vacuo vibration test.

The flutter stability of the linearized aeroelastic model is considered by solving Eq. (11). The aeroelastic eigenvalues obtained from these equations determine the stability of the system. When the real part of any one eigenvalue λ becomes positive, the entire system becomes unstable.

Figure 3 shows a typical graphical representation of the eigenanalysis in the form of real eigenvalues $Re(\lambda_i)$ (damping) vs the flow velocity for $\alpha_0 = 0$ and 0.1 deg. As indicated by the symbol • for $\alpha_0 = 0.1$ deg, there are two intersections of $Re(\lambda_i)$ with the velocity axis at $U_f = 44$ m/s (lower instability flutter boundary) and 84.8 m/s (upper boundary), and the corresponding flutter oscillatory frequencies are $\omega_f = 25.1$ and 42 Hz. Below the lower and above the upper flutter velocities, the system is stable. For $\alpha_0 = 0$ deg, the

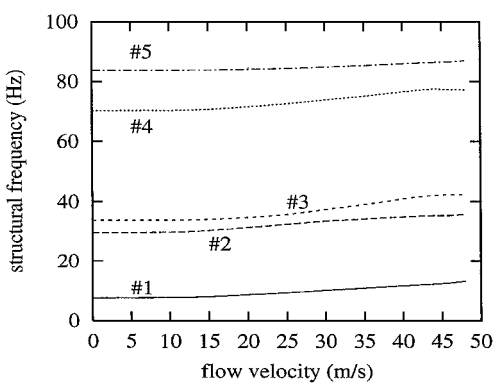

Fig. 2 Structural frequencies vs flow velocity for $\alpha_0 = 0.1$ deg.

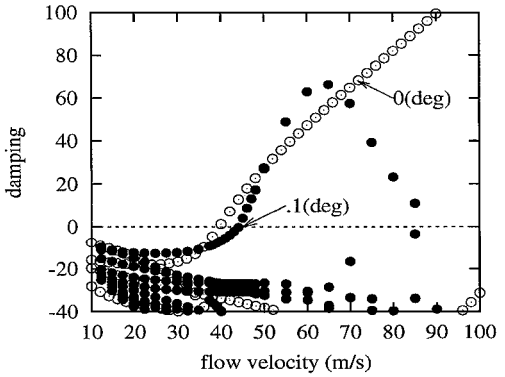

Fig. 3 Eigenvalue solutions of the linearized aeroelastic model for $\alpha_0 = 0$ and 0.1 deg.

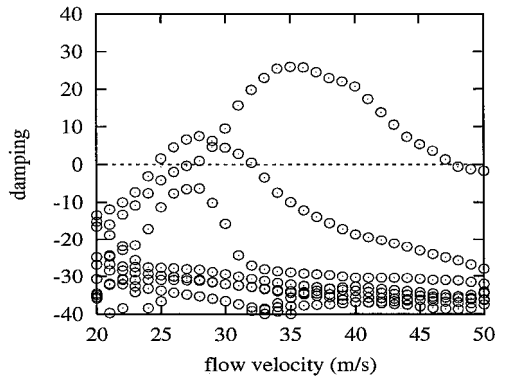

Fig. 4 Eigenvalue solutions of the linearized aeroelastic model for $\alpha_0 = 0.75$ deg.

corresponding lower flutter values are $U_f = 39.7$ m/s and $\omega_f = 21.7$ Hz. There is no upper instability flutter boundary for $\alpha_0 = 0$ deg, i.e., beyond the critical flutter velocity, the system is always unstable. These latter results are indicated by the symbol ∘. The critical flutter velocity and frequency for $\alpha_0 = 0.1$ deg are higher by 11 and 16%, respectively, than those for $\alpha_0 = 0$ deg.

These results obtained from the dynamic perturbation Eq. (11) can be confirmed by the results calculated by the time marching approach of Eq. (7). At $U = 44.1$ m/s, the response approaches a small limit cycle oscillation amplitude (for a detailed discussion, see the next section). The flow velocity is slightly higher than the flutter velocity, $U_f = 44$ m/s, and the oscillation frequency is close to the flutter frequency. Thus it is confirmed that $U = 44$ m/s is a true flutter velocity.

2. Results for $\alpha_0 = 0.3$ deg and higher

For $\alpha_0 = 0.3$ deg, we find there are three intersections of $Re(\lambda_i)$ with the velocity axis at $U = 37$, 65.8, and 68 m/s, i.e., the flutter velocities, and the corresponding flutter oscillatory frequencies of $\omega_f = 36.9$, 50.4, and 76 Hz. The first two flutter velocities form an instability flutter range dominated by coupling between the first two structural modes. Beyond the flutter velocity $U_f = 68$ m/s, the system enters another instability flutter range dominated by coupling between the higher structural modes.

For $\alpha_0 = 0.5$ deg, similar results are found. There are three instability flutter ranges in this case. The first instability range is from $U = 30$ to 46.8 m/s, and the corresponding frequencies vary from $\omega_f = 39$ to 47 Hz. The motion is dominated by coupling between the first two structural modes. The second and third instability ranges are from $U = 43.5$ to 47 m/s and 48.5 to 54 m/s, and the corresponding frequencies vary from $\omega_f = 123$ to 130 Hz and 97.8 to 100 Hz, respectively. These are dominated by coupling between higher structural modes.

If the steady angle of attack increases again from $\alpha_0 = 0.5$ deg, it is expected the lowest flutter velocity will be decreased. For $\alpha_0 = 0.75$ deg, there are two flutter ranges as shown in Fig. 4. One is from $U = 24.5$ to 32 m/s, and the corresponding frequencies vary

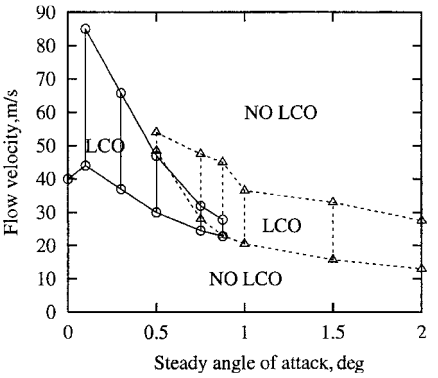

a) Flutter boundary

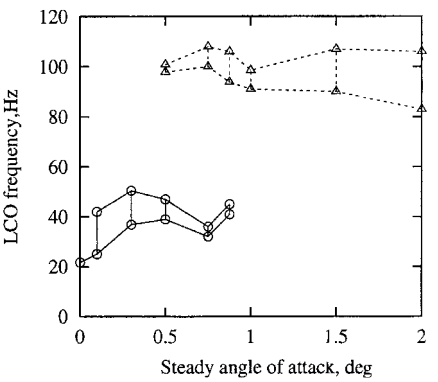

b) Flutter frequency

Fig. 5 Linearized flutter characteristics vs a steady angle of attack.

from $\omega_f = 32$ to 36 Hz and the motion is dominated by the coupling between first two structural modes. The other is from $U = 28$ to 47.5 m/s and the corresponding frequencies vary from $\omega_f = 100$ to 108 Hz and is dominated by higher structural mode coupling. In this case, the latter instability becomes stronger and the lower flutter range becomes weaker as compared with the results for $\alpha_0 = 0.3$ and 0.5 deg. When $\alpha_0 = 1$ deg, the lower flutter range disappears, the higher instability flutter range is between $U = 20.5$ and 36.5 m/s, and the corresponding frequencies vary from $\omega_f = 91$ to 98.5 Hz. These relationships mean that the flutter mode is dominated by coupling of higher structural natural modes rather than coupling of the first and second structural natural modes. Similar results are found up to $\alpha_0 = 2$ deg. In this case, a higher flutter range is seen beyond $U = 28.5$ m/s with corresponding flutter frequency $\omega_f = 215$ Hz, in addition to the original higher flutter range from $U = 13$ to 27.5 m/s and $\omega = 83$ to 106 Hz.

Summarizing the above results, a relationship between the first two flutter boundary ranges and the steady angle of attack is obtained as shown in Fig. 5a. Figure 5b shows the corresponding flutter frequency ω_f vs α_0. The lower mode flutter boundary ranges are indicated by the symbol ∘ with a solid line, and the higher mode flutter boundary ranges are indicated by the symbol △ with a dashed line. Note that the flutter behavior has a transition of flutter mode near $\alpha_0 = 1$ deg. The flutter velocity is sensitive to the steady angle of attack in the range of $\alpha_0 = 0 \rightarrow 2$ deg.

B. Limit Cycle Oscillations

We have used a standard discrete time algorithm to calculate the nonlinear response of this aeroelastic system using Eq. (10). The time step Δt is constant for a given flow velocity U. Typically $U\Delta t/\Delta x = \frac{1}{4}$ to $\frac{1}{15}$. As U increases, Δt is decreased to avoid numerical divergence. An LCO is observed at velocities higher than the lowest linear perturbation flutter velocity but not below the flutter velocity.

A typical nondimensional transverse displacement time history and corresponding fast Fouier transform (FFT) at, $x = 1$, $y = 1$, $U = 46$ m/s $> U_f$, and $\alpha_0 = 0.1$ deg are shown in Figs. 6a and 6b by a solid line. There is a steady-state limit cycle oscillation with dominant frequency of $\omega = 25.5$ Hz. Note that the linear flutter velocity

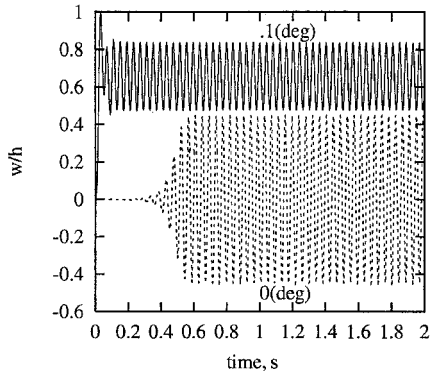

a) Time history

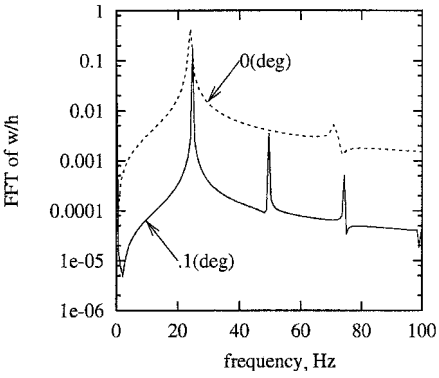

b) FFT analysis

Fig. 6 Limit cycle oscillations of nondimensional transverse deflection for $\alpha_0 = 0$, 0.1 deg, and $U = 46$ m/s.

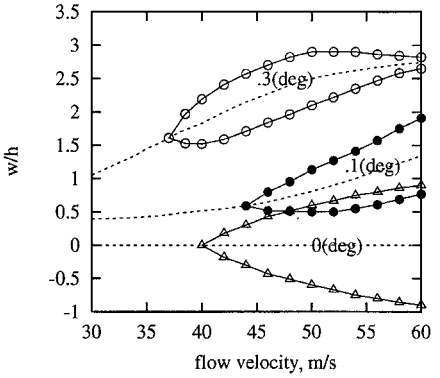

a) LCO amplitude

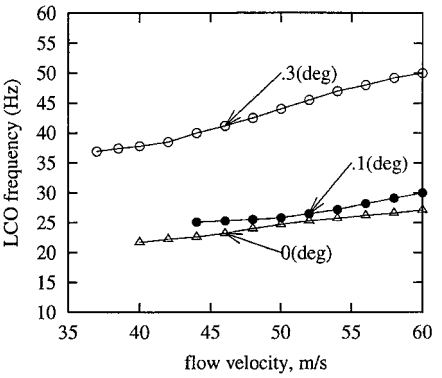

b) Oscillation frequency

Fig. 7 Limit cycle peak amplitudes vs flow velocity U for $\alpha_0 = 0$, 0.1, and 0.3 deg at the tip of wing.

and frequency are $U_f = 44$ m/s and $\omega_f = 25.1$ Hz. For comparison, the results for $\alpha_0 = 0$ are also plotted in this figure, indicated by a dashed line, for the same velocity.

Figure 7a shows the nondimensional transverse peak amplitude of the limit cycle oscillation vs the flow velocity for $\alpha_0 = 0.1$ and 0.3 deg. For comparison, the result for $\alpha_0 = 0$ is also plotted in this figure. As U increases, both static amplitudes (as indicated by a dashed line) and dynamic amplitudes (indicated by the symbols ●, ○) increase for $\alpha_0 = 0.1$ and 0.3 deg. No static deflection occurs for $\alpha_0 = 0$, but the dynamic amplitudes indicated by the symbol △ are larger than those for $\alpha_0 = 0.1$ and 0.3 deg. The LCO is almost single harmonic motion as shown in Fig. 6. Figure 7b shows the corresponding oscillation frequency of LCO vs the flow velocity. The oscillation frequency for $\alpha_0 = 0.1$ deg is slightly higher than that for $\alpha_0 = 0$. However, for $\alpha_0 = 0.3$ deg, the oscillation frequency is notably higher than that for $\alpha_0 = 0$ and 0.1 deg.

Figure 8a shows the nondimensional transverse peak amplitude of the LCO vs the flow velocity for $\alpha_0 = 0.5$, 0.75, and 1 deg. As U increases, the static deflection (as indicated by a dashed line) increases for all cases. The dynamic amplitude for $\alpha_0 = 0.5$ deg (indicated by the symbols ●) increases and then decreases. The maximum value corresponds to $U = 38$ m/s. The oscillation frequency (Fig. 8b) also increases but is dominated by the lower flutter mode frequency.

For $\alpha_0 = 0.75$ deg, there is a jump phenomenon between $U = 32$ and 34 m/s, both in the LCO dynamic amplitude and oscillation frequency, as indicated by the solid line. The amplitude drops from about 0.12 to 0.01, and the frequency jumps from about 40 to 100 Hz. These results are explained by Fig. 4. The velocity $U = 32$ m/s is the upper critical point for the lowest flutter mode. In the range of $U > 32$ m/s, the flutter is dominated by higher flutter mode with $\omega_f = 100$ Hz. The LCO corresponding to the higher flutter mode is weak, however. Typical FFT analysis for $U = 27$ m/s (lower LCO mode) and for $U = 34$ m/s (higher LCO mode) is shown in Fig. 9. As shown in Fig. 9, the solid line indicates the results for $U = 27$ m/s with an oscillation frequency $\omega = 35$ Hz and a peak amplitude about 0.1. The dashed line is for $U = 34$ m/s with an oscillation frequency $\omega = 107$ Hz and a peak amplitude of about 0.01.

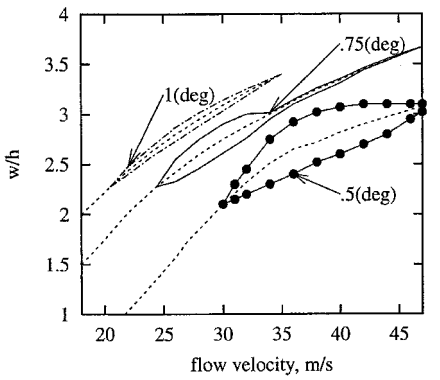

a) LCO amplitude

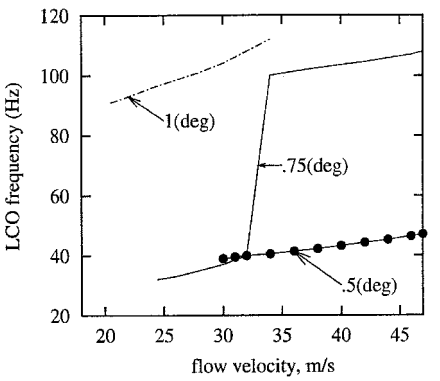

b) Oscillation frequency

Fig. 8 Limit cycle peak amplitudes vs flow velocity U for $\alpha_0 = 0.5$, 0.75, and 1.0 deg at the tip of wing.

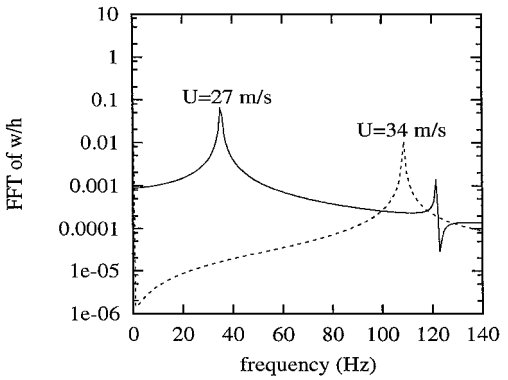

Fig. 9 FFT analysis of limit cycle oscillations for $U = 27$, 34 m/s, and $\alpha_0 = 0.75$ deg at the tip of wing.

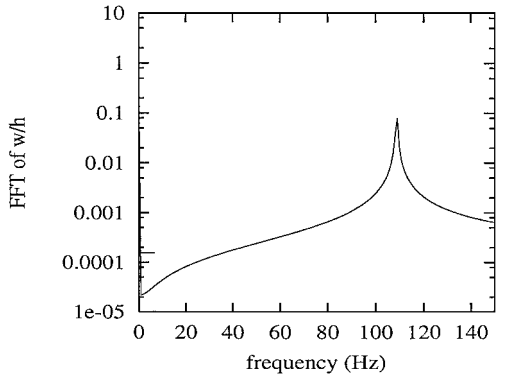

Fig. 10 FFT analysis of limit cycle oscillations for $U = 30$ m/s and $\alpha_0 = 1.0$ deg at the tip of wing.

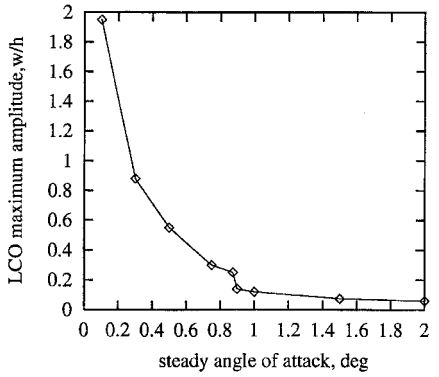

a) Oscillation frequency

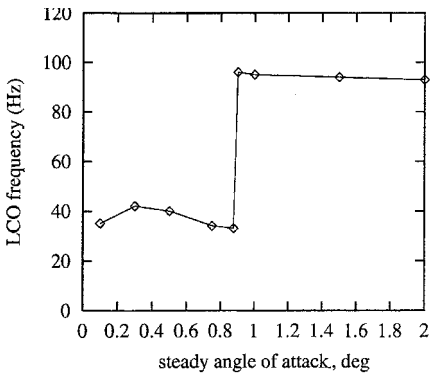

b) Steady angle of attack

Fig. 11 Maximum nondimensional LCO peak-to-peak amplitudes.

For $\alpha_0 = 1$ deg, the flutter is dominated by the higher flutter mode. The lower flutter boundary is $U_f = 20.5$ m/s with $\omega_f = 91$ Hz, and the upper one is $U_F = 36.5$ m/s with $\omega_f = 98.5$ Hz. The LCOs occur between the lower and upper flutter boundaries. The amplitude of the LCO is very small compared with those for $\alpha_0 < 0.5$ deg, as indicated by the dotted line in Fig. 8. A typical FFT analysis for $U = 30$ m/s is shown in Fig. 10. This figure shows a simple harmonic oscillation with a frequency $\omega = 108$ Hz and peak amplitude about 0.1.

Summarizing the above results, a relationship between the maximum peak-to-peak amplitude and oscillation frequency of LCOs and the steady angle of attack is obtained as shown in Figs. 11a and 11b, respectively. The amplitude decreases as the steady angle of attack increases, and there is a change in the LCO mode for α_0 near 1 deg. Such effects have been observed in flight flutter experiments.[5]

V. Conclusion

The present paper provides new insights into nonlinear aeroelastic phenomena not previously widely appreciated, i.e., LCOs for low aspect ratio wings that have a platelike structural behavior. The effects of a steady angle of attack on both the flutter instability boundary and the LCO are significant. For a small steady angle of attack, $\alpha_0 \leq 0.1$ deg, the flutter onset velocity increases whereas for larger α_0, it decreases. Moreover, as α_0 increases, the maximum LCO amplitude decreases substantially.

Appendix: Coefficient Matrices

$$C^u_{i,j} = 12\frac{c}{h}\left[\iint_s \frac{\partial U_i}{\partial x}\frac{\partial U_j}{\partial x}\,dx\,dy + \frac{(1-\nu)}{2}\left(\frac{c}{L}\right)^2 \iint_s \frac{\partial U_i}{\partial y}\frac{\partial U_j}{\partial y}\,dx\,dy\right]$$

$$C^v_{i,j} = 12\frac{c}{L}\frac{c}{h}\left[\nu\iint_s \frac{\partial V_i}{\partial y}\frac{\partial U_j}{\partial x}\,dx\,dy + \frac{(1-\nu)}{2}\iint_s \frac{\partial V_i}{\partial x}\frac{\partial U_j}{\partial y}\,dx\,dy\right]$$

$$C^q_{i,km} = -6\iint_s \left(\frac{\partial W_k}{\partial x}\frac{\partial W_m}{\partial x}\frac{\partial U_i}{\partial x} + \nu\left(\frac{c}{L}\right)^2 \frac{\partial W_k}{\partial y}\frac{\partial W_m}{\partial y}\frac{\partial U_i}{\partial x} + (1-\nu)\left(\frac{c}{L}\right)^2 \frac{\partial W_k}{\partial x}\frac{\partial W_m}{\partial y}\frac{\partial U_i}{\partial y}\right)dx\,dy$$

$$D^u_{i,j} = 12\frac{c}{h}\left[\nu\iint_s \frac{\partial V_i}{\partial y}\frac{\partial U_i}{\partial x}\,dx\,dy + \frac{(1-\nu)}{2}\iint_s \frac{\partial V_i}{\partial x}\frac{\partial U_j}{\partial y}\,dx\,dy\right]$$

$$D^v_{i,j} = 12\frac{L}{h}\left[\left(\frac{c}{L}\right)^2\iint_s \frac{\partial V_i}{\partial y}\frac{\partial V_j}{\partial y}\,dx\,dy + \frac{(1-\nu)}{2}\iint_s \frac{\partial V_i}{\partial x}\frac{\partial V_j}{\partial x}\,dx\,dy\right]$$

$$D^q_{i,km} = -6\iint_s \left(\left(\frac{c}{L}\right)^2 \frac{\partial W_k}{\partial y}\frac{\partial W_m}{\partial y}\frac{\partial V_i}{\partial y} + \nu\frac{\partial W_k}{\partial x}\frac{\partial W_m}{\partial x}\frac{\partial V_i}{\partial y} + (1-\nu)\frac{\partial W_k}{\partial x}\frac{\partial W_m}{\partial y}\frac{\partial V_i}{\partial x}\right)dx\,dy$$

$$M^k_m = \iint_s W_m W_k\,dx\,dy$$

$$\Pi^1_{l,ik} = 12\frac{c}{h}\iint_s \begin{pmatrix} \partial W_l & \partial W_k & \partial U_i \\ \partial x & \partial x & \partial x \end{pmatrix} + \nu\left(\frac{c}{L}\right)^2 \begin{pmatrix} \partial W_l & \partial W_k & \partial U_i \\ \partial y & \partial y & \partial x \end{pmatrix}$$

$$+ 0.5(1-\nu)\left(\frac{c}{L}\right)^2 \begin{pmatrix} \partial W_l & \partial W_k & \partial U_i \\ \partial x & \partial y & \partial y \end{pmatrix}$$

$$+ 0.5(1-\nu)\left(\frac{c}{L}\right)^2 \begin{pmatrix} \partial W_l & \partial W_k & \partial U_i \\ \partial y & \partial x & \partial y \end{pmatrix} \mathrm{d}x\,\mathrm{d}y$$

$$\Pi^1_{l,jk} = 12\frac{c^2}{Lh}\iint_s \left(\left(\frac{c}{L}\right)^2 \begin{pmatrix} \partial W_l & \partial W_k & \partial V_j \\ \partial y & \partial y & \partial y \end{pmatrix} + \nu \begin{pmatrix} \partial W_l & \partial W_k & \partial V_j \\ \partial x & \partial x & \partial y \end{pmatrix}\right.$$

$$+ 0.5(1-\nu) \begin{pmatrix} \partial W_l & \partial W_k & \partial V_j \\ \partial x & \partial y & \partial x \end{pmatrix}$$

$$\left. + 0.5(1-\nu) \begin{pmatrix} \partial W_l & \partial W_k & \partial V_j \\ \partial y & \partial x & \partial x \end{pmatrix}\right) \mathrm{d}x\,\mathrm{d}y$$

$$\Pi^2_{l,kmn} = 6\iint_s \begin{pmatrix} \partial W_l & \partial W_k & \partial W_m & \partial W_n \\ \partial x & \partial x & \partial x & \partial x \end{pmatrix}$$

$$+ \left(\frac{c}{L}\right)^4 \begin{pmatrix} \partial W_l & \partial W_k & \partial W_m & \partial W_n \\ \partial y & \partial y & \partial y & \partial y \end{pmatrix}$$

$$+ \left(\frac{c}{L}\right)^2 \begin{pmatrix} \partial W_l & \partial W_k & \partial W_m & \partial W_n \\ \partial y & \partial y & \partial x & \partial x \end{pmatrix}$$

$$+ \left(\frac{c}{L}\right)^2 \begin{pmatrix} \partial W_l & \partial W_k & \partial W_m & \partial W_n \\ \partial x & \partial x & \partial y & \partial y \end{pmatrix} \mathrm{d}x\,\mathrm{d}y$$

$$[\mathcal{A}] = \begin{pmatrix} I & -Y^T_{\mathrm{Ra}}[I - A(A+B)^{-1}]TE \\ C_2 X_{\mathrm{Ra}} & D_2 + C_2(A+B)^{-1}TE + K_d\,|\,2\tau^2 \end{pmatrix}$$

$$[\mathcal{B}] = \begin{pmatrix} -Z_{\mathrm{Ra}} & Y^T_{\mathrm{Ra}}B(A+B)^{-1}TE \\ C_1 X_{\mathrm{Ra}} & D_1 + C_1(A+B)^{-1}TE + K_d\,|\,2\tau^2 \end{pmatrix}$$

Acknowledgments

This work was supported under the Air Force Office of Scientific Research grant "Limit Cycle Oscillations and Nonlinear Aeroelastic Wing Response." Brian Sanders and, currently, Daniel Segalman have served as the Grant Program Officer. All numerical calculations were done on a supercomputer, T916, in the North Carolina Supercomputing Center.

References

[1] Doggett, R. V., and Solstmann, D. L., "Some Low-Speed Flutter Characteristics of Simple Low-Aspect-Ratio Delta Wing Models," NASA TM 101547, Jan. 1989.

[2] Tang, D. M., Dowell, E. H., and Hall, K. C., "Limit Cycle Oscillations of a Cantilevered Wing in Low Subsonic Flow," *AIAA Journal*, Vol. 37, No. 3, 1999, pp. 364–371.

[3] Tang, D. M., Henry, J. K., and Dowell, E. H., "Limit Cycle Oscillations of Delta Wing Models in Low Subsonic Flow," *AIAA Journal*, Vol. 37, No. 11, 1999, pp. 1355–1362.

[4] Hall, K. C., "Eigenanalysis of Unsteady Flows About Airfoils, Cascades, and Wings," *AIAA Journal,* Vol. 32, No. 12, 1994, pp. 2426–2432.

[5] Bunton, R. W., and Denegri, C. M., Jr., "Limit Cycle Oscillation Characteristics of Fighter Aircraft," *Journal of Aircraft*, Vol. 37, No. 5, 2000, pp. 916–918.

E. Livne
Associate Editor